OE Optical Engineering

RESEARCH PAPER

Design, modeling, fabrication, and characterization of 50 mm diameter focus tunable liquid crystal lens with enhanced optical performance

Amit K. Bhowmick,[a] Afsoon Jamali,[b] Douglas Bryant,[a] Sandro Pintz,[b] and Philip J. Bos[a,*]

[a]Kent State University, Material Science Graduate Program, Kent, Ohio, United States
[b]Meta Platforms Inc., Reality Lab, Redmond, Washington, United States

ABSTRACT. In prior research, Jamali et al. demonstrated the efficacy of a 20-mm aperture liquid crystal (LC) tunable lens for both accommodation-convergence mismatch correction and presbyopia correction. This lens employed a concentric ring electrode-based LC design with a segmented phase profile, enabling a larger aperture size without affecting switching speed. However, for near-eye application, a high optical quality LC lens with larger than 20-mm aperture size is a requirement to allow large field of view. Therefore, we report here a 50-mm aperture LC lens with incorporated solutions to minimize haze that results due to the large aperture size. Due to its large aperture size, fast switching speed, compact size, and low voltage operation, the reported 50 mm LC lens is a practical option for near-to-eye applications and other tunable lens applications. The objective of this paper is to provide a comprehensive detail on the design, modeling, fabrication, and characterization of the optical quality of the developed 50 mm LC lens. Quantitative assessments of the lens's optical quality are presented across the entire aperture, with a particular focus on near-eye applications.

Keywords: electroptics; tunable lens; AR/VR; liquid crystals

Paper 20240416G received Apr. 22, 2024; revised Jun. 17, 2024; accepted Jun. 21, 2024; published Jul. 27, 2024.

1 Introduction

Large-area tunable lenses have gained significant attention for diverse near-eye applications, including accommodation-convergence (AC) correction in emerging head-mounted displays (HMDs),[1] ophthalmic applications, such as presbyopia correction,[2–5] eyeglass applications,[6–8] wavefront correction,[9] and light control.[10] Despite the growing interest, no existing technology fully satisfies all the specifications required for near-eye displays. These requirements span low voltage, lightweight, compactness, continuous tunability, fast switching speed, and more.[11] Among various approaches, liquid crystal (LC) tunable lens technology stands out due to its low power consumption, stability, compactness, and cost-effectiveness. Developing large-aperture LC tunable lenses that offer rapid switching speeds and high optical quality presents significant challenges. Previous reports have discussed polarization-independent multi-electrode lenses using blue-phase LC, but these typically require high operational voltages and lack large aperture size.[12] Various techniques have been explored to improve these lenses, including the use of discrete ring electrodes and resistive electrodes. These methods have been extensively

*Address all correspondence to Philip J. Bos, pbos@kent.edu

studied for their precise control over the tunable phase profile, achieving diffraction-limited performance.[13] Despite these advancements, the maximum aperture size of high-quality refractive lenses has been limited to 2.4 mm, which is inadequate for certain applications.[14] To address these limitations, Jamali et al. have developed a new approach, introducing a fast-switching (<1 s), continuously tunable LC lens with a diameter of 2 cm.[15] This design utilized concentric ring electrodes and a segmented phase profile (SPP) concept, showing promise for realizing larger aperture lenses (>2 cm) without compromising switching speed. However, inherent trade-offs exist in this approach, notably related to haze caused by phase discontinuity at the edge of concentric electrodes and the boundaries of segmented phase resets. Recent work has analyzed these optical artifacts using numerical simulations and proposed approaches to mitigate them.[16]

In this study, we present a detailed design, modeling, fabrication, and characterization of a continuously tunable (1.60 D tunable range) 5 cm diameter GRIN LC lens. Our design is based on concentric ring electrodes and an SPP.[15] Further, we have implemented solutions to reduce haze and discuss the fabrication details and characterization of the built device in this report.

2 Design

In this section, we discuss the design parameters of a 5 cm diameter LC lenses, where the optical power ranges from −0.80 D to +0.80 D. A fixed power glass lens of +0.80 D is stacked with the LC lens as a bias lens to shift the tunable optical power range to be from 0 D to 1.60 D, similar to the approach shown by Fan et al.[17] Considering the viewing angle issue that can occur for a single LC cell, the lens is a stack of two anti-parallel rubbed LC cells to correct for this issue,[15] where each LC cell in our example design has a power range of ±0.40 D. Jamali et al. previously demonstrated the effectiveness of the anti-parallel rubbed cell stacking for viewing angle performance.[15] Since the two LC cells in the stack are identical in design and construction, the performance characterization and modeling of the lens are collectively represented as a lens, rather than analyzing each cell individually.

For a 5-cm diameter lens, the maximum OPD required to achieve +0.80 D optical power can be calculated from Eq. (1), which gives maximum OPD is ∼250 μm or 448λ (where λ is the design wavelength of 543.5 nm). The OPD varies in a parabolic phase profile across the entire aperture, as shown in Fig. 1. To achieve this maximum OPD of 448λ, the required cell thickness of the LC lens can be calculated using Eq. (2). However, using an LC material with a Δn value of 0.29 would result in a required cell thickness of ∼860 μm, which would significantly affect the device's response speed. To overcome this issue, 28 SPP is implemented to reduce the thickness of the lens.[15] When utilizing 75% of the total optical swing of a LC material with a birefringence of 0.29, the necessary thickness of the cell for the SPP LC lens is reduced to 20 μm. As a result, OPD in each segmented phase region is 16λ. The SPP OPD profile of the LC lens is shown in Fig. 1(a) with a blue curve:

$$\mathrm{OPD}_{\text{thin lens}} = \frac{r^2}{2f}, \tag{1}$$

$$\mathrm{OPD}_{\mathrm{LC}} = \Delta n d. \tag{2}$$

The LC lens provided as an example is polarization dependent, as it is designed to alter only the extraordinary refractive index. Nonetheless, polarization independence can be attained by stacking another LC lens with an orthogonal rubbing direction.[18]

In the designed LC lens, a 2 μm electrode gap is used between driving electrodes. Floating electrodes, and an additional insulator layer on top of the floating electrodes to minimize light scattering due to that gap.[13]

In previous studies, the switching speed of the LC lens with 28 SPP technology was measured and found to be ∼500 ms for a full optical power shift from 0 D to 1.60 D. However, the response speed could be further enhanced by optimizing the driving scheme, such as through the application of voltage overshoot methods.[19,20] In addition, the design of our LC lens allows for continuous focal length adjustment, which provides a significant advantage in terms of switching speed. For example, instead of jumping directly from 0 D to 1.60 D, our lens can incrementally

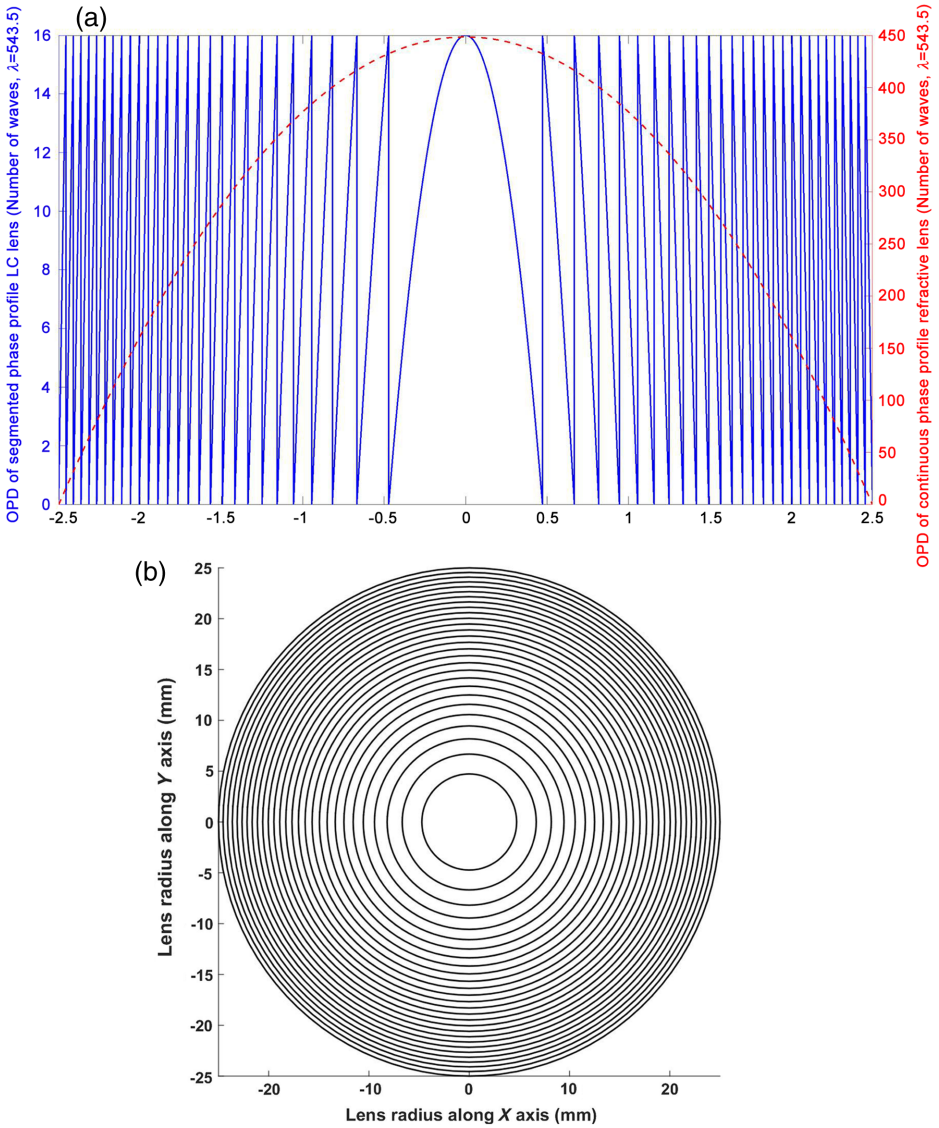

Fig. 1 (a) Design of phase profile of an SPP LC lens with 28 segmented phase regions compared to an ideal refractive type lens of similar power. The blue solid and red dashed color curves represent LC lens and continuous parabolic shape phase profile ideal lens, respectively. (b) Top view of the segmented phase region of the 5 cm lens. The black circles within the width of the lens represent the position of the phase resets.

adjust the optical power in steps of 0.1 D, allowing for smoother transitions and potentially faster response times.

3 Modeling

3.1 Defining the System

The average size of the human eye pupil (HEP) is around 5 mm,[21] whereas the designed lens aperture size is 50 mm. Due to this 10-fold difference in aperture size, different pupil positions (PPs) are adopted for modeling and characterizing the lens. These PPs correspond to various gazing angles of the HEP. As the example lens is designed for near-eye applications, it was assumed that the position of the LC lens is 2 cm away from the HEP. Consequently, five PPs are defined, namely PP1, PP2, PP3, PP4, and PP5, corresponding to center of gazing angles of 0 deg, 14 deg, 27 deg, 36 deg, and 46 deg, respectively. The number of SPPs for these PPs will vary due to the parabolic change in width of the SPP in the radial direction. Figure 2 shows the

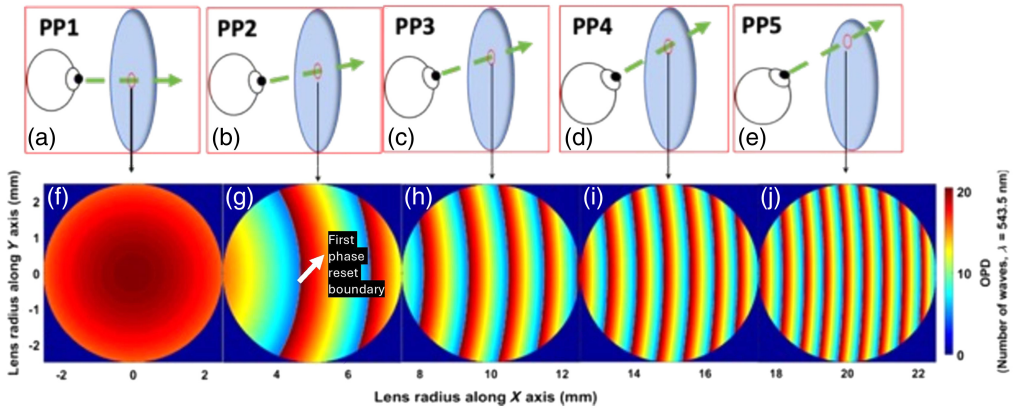

Fig. 2 Illustration of different PPs and the corresponding 2D phase profile on the lens surface. (a)–(e) PP1, PP2, PP3, PP4, PP5, respectively. Center of gazing angle of 5 mm pupil for (a)–(e) are 0 deg, 14 deg, 27 deg, 36 deg, and 46 deg, respectively. (f)–(j) The 2D phase map on the LC lens for PP1, PP2, PP3, PP4, PP5, respectively. The color shows the phase change with lens area. Each phase reset gives stepwise increase of 16λ of optical path difference.

five PPs and the corresponding 2D phase map on the surface of the example LC lens. Out of five PPs, only PP1 represents the central view of the user.

3.2 Numerical Point Spread Function

The use of an SPP affects the optical quality of the lens. In an ideal case, the phase change from one segmented phase region to the next should be a module of 2π for maximum diffraction efficiency, and there should be a sharp phase step by $(2\pi * 8)$ radians at the phase reset. However, in an actual device, there is an effect of the fringing electric field between the neighboring discrete ring electrodes around the phase resets. As a consequence, there is light scattering from phase resets and an effective amplitude grating problem. This issue is considered in a previous paper[16] where a light absorbing layer (black mask "BM') is proposed to reduce light scattering. While the light scattering effect can be improved with BM, the amplitude grating issue still remains and causes significant drop in diffraction efficiency.

In the presence of the BM, the PSFs are simulated for the example 5 cm lens and are shown in Fig. 3 for all PPs, providing a quantitative measurement of optical quality throughout the entire lens aperture. The PSFs are calculated for the best-case scenario, when the phase step condition at the reset is an integer multiple of the wavelength of light [Figs. 3(a)–3(e)], and the worst-case scenario, when the phase step condition at the reset is a half-integer multiple of the wavelength of light [Figs. 3(f)–3(j)]. In worst case, the incident beam splits into two diffracted beams due to destructive interference. If one of the diffracted beams splits at angle $+\theta$ and other at $-\theta$, the angle θ can be written as

$$\theta = \sin^{-1}\left(\frac{\lambda}{2\Lambda}\right), \tag{3}$$

where Λ is the periodicity of the segmented phase region. The angle of the diffracted beam in such a case is approximately inversely proportional to the periodicity of the segmented phase width, which is reflected in the PSF modeling (Fig. 3). However, regardless of the phase step condition of the SPP, a continuous decrease in spot profile resolution is observed as the gazing angle increases across the aperture area. This phenomenon can be attributed a dominant amplitude grating issue. In particular, a significant drop in spot profile resolution is observed beyond a viewing angle of 30 deg for any phase step condition in the SPP design, where the width of the segmented phase region is <1 mm in the example lens design. The Strehl ratio (SR) is determined by comparing the peak intensity of the diffraction-limited spot profile to the peak intensity of the observed spot profile. The calculated SR for each spot profile is shown in Fig. 3.

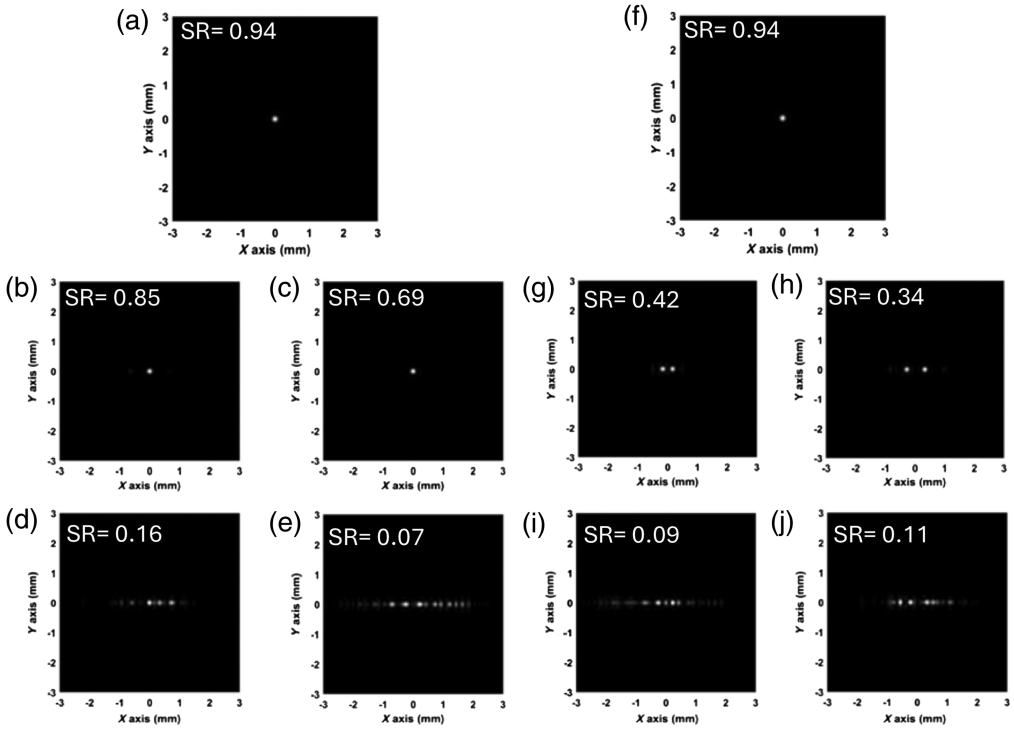

Fig. 3 Modeled PSF of the designed lens at designed wavelength, $\lambda = 543.5$ nm when phase step is multiple of one wave [(a) to (e) for PP1, PP2, PP3, PP4, PP5, respectively] and non-designed wavelength when phase step is multiple of half-wave [(f) to (j) for PP1, PP2, PP3, PP4, PP5, respectively] including the BM. The calculated SR is indicated in each subfigure.

3.3 Numerical Modulation Transfer Function

The modulation transfer function (MTF) for different PPs is calculated by taking the Fourier transform of each calculated PSF, as shown in Fig. 4. More details of this method for obtaining the PSF from the near-field phase profile are discussed in Ref. 22.

3.4 SPP Lens Performance and Human Perception

The evaluation of optical performance can be done by considering multiple factors. First, diffraction can be minimized if the phase increment is an integer multiple of the viewing light's

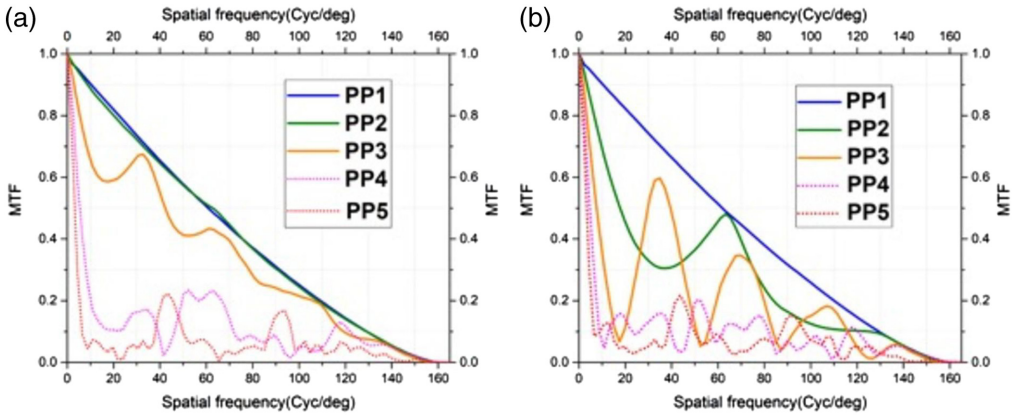

Fig. 4 Simulated MTF of the designed lens at different PP. (a) At maximum diffraction efficient, when viewing wavelength (λ) of light cause phase steps in the segmented resets to be multiple of one wave (Phase step $= N_{\max}\lambda$, where $N_{\min} = 1,2,3,\ldots$), (b) at minimum diffraction efficiency, when viewing wavelength (λ) of light cause phase steps in the segmented resets to be multiple of half-wave (phase step $= N_{\min}\lambda$, where $N_{\min} = \frac{1}{2},\frac{3}{2},\frac{5}{2},\ldots$).

optical path difference. For the SPP lens, the phase change is optimized for green light ($\lambda = 543.5$ nm), which is most sensitive to the human eye. Second, within the first phase reset (width ~10 mm) at the lens center, diffraction-limited performance can be achieved irrespective of the viewing light wavelength. Assuming the lens is placed 20 mm from the subject, this region covers a viewing angle within ± 15 deg. Third, the worst-case diffraction performance occurs above the field of view of the first phase reset region, when the phase step increment on the reset boundaries is a half-integer multiple of the wavelength. In such cases, the outgoing beam splits into two, but if the angle between them is less than the human eye's angular resolution of 1 arcmin, the diffracted image cannot be distinguished by the user. Based on the PSF, it is observed angle between the diffracted beams is still within human eye resolution within PP3, covering area of ± 30 deg of gazing angle where the width of the segmented phase regions within this area is greater than 1 mm. Fourth, it can been seen from the simulated data, chromatic aberrations become unavoidable at higher gazing angles when using white light. However, research by Zhan et al. has demonstrated an effective approach to correct these aberrations.[23] Finally, numerous studies have shown that easy eye rotation angle lies between ± 30 deg gazing angle for horizontal and vertical vision, beyond this limit user tends to move their head for comfortable vision.[24]

4 Fabrication

4.1 Driving Scheme

In the device, the main goal is to achieve good parabolic phase profile across entire lens aperture with simplified driving mechanism. Like Li et al.,[25] Rize et al.,[26] and Naumov et al.,[27] we utilize a resistive network in the discrete ring electrodes to minimize the number of external connections. In such driving scheme, every ring electrode is internally connected by an inter-ring resistor to provide a linear voltage drop across adjacent electrodes. Current flow from one electrode to the next electrodes, hence, acts as voltage divider circuit.

To drive the lens, we utilized eight input voltages due to non-linear relationship between applied voltage and phase change in LC material. The driving voltages are named as busline voltages. The OPD versus voltage curve is linear between two busline voltage values. The busline voltages only make connection to the addressable electrodes though a via interconnect. The electrodes between the addressable electrodes cause voltage to drop due to the inner ring resistors. The value of resistors and via positions are selected in such a way that the voltage drop on several electrodes between addressable ring electrode is linear. To create the SPP, the same voltage distribution is repeated in each segmented phase region.

In the patterned first layer of ring electrodes, there is a gap between electrodes where a weak electric field originates from the edge of the electrodes. Such a relatively weaker electric field in the electrode gap area creates a phase bump in that region. As discussed in Ref. 16, to reduce the phase bump at the electrode gap, the second layer of electrodes (floating electrodes) is implemented on top of the gaps of the first pattern indium tin oxide (ITO) layer.

Figure 5(a) displays the top view of the mask diagram of the build LC lens, which includes all the layers. The green and orange regions represent the busline connection and concentric electrodes, respectively. In addition, black color rings on top of electrodes in Fig. 5(a) indicate the positions of the SPP resets. Figure 5(b) provides a closer view of the first patterned ITO layer at the center of the lens, while Fig. 5(c) shows a closer view of the same area, including the second layer of ITO (floating electrodes).

4.2 Fabrication Steps

The basic fabrication process is similar to previous devices, but additional layers are implemented in this device to improve the optical performance. Specifically, the solutions described (insulator layer on top of floating electrode and black mask) in earlier report[16] are implemented in the fabrication process.

Each cell comprises two glass plates coated with ITO that sandwich an LC material. The bottom glass plate features patterned driving electrode structures with an inter-ring resistor network, while the top plate contains a ground electrode with a patterned black matrix (BM) layer.

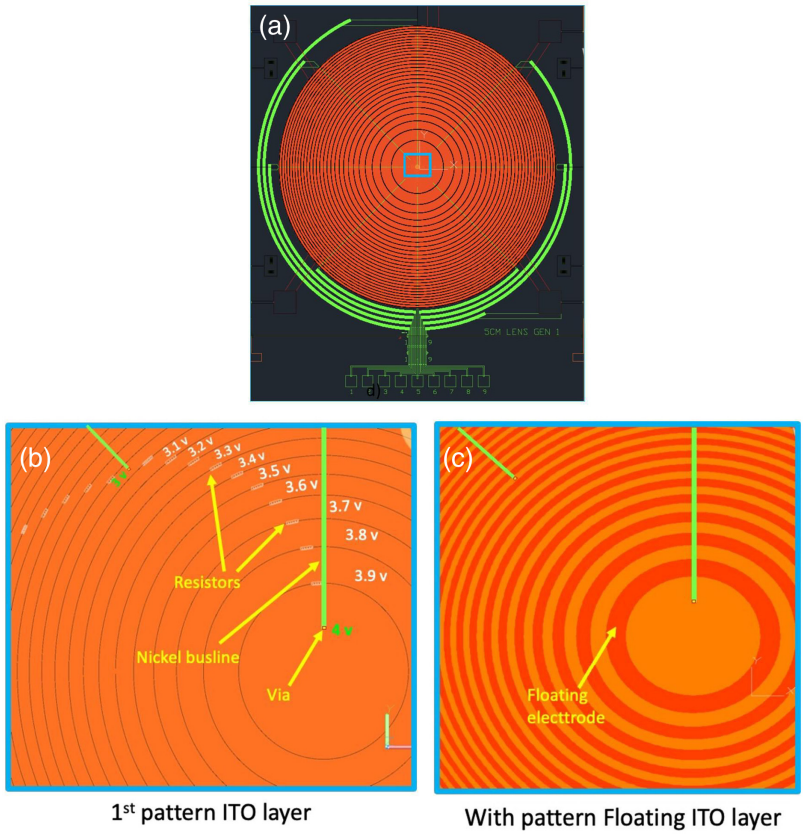

Fig. 5 (a) Mask diagram of the 5 cm focus tunable LC lens. Green, orange, and black colors are representing the driving busline channels, ITO concentric ring electrodes, positions of the phase resets. Closer look at within the central blue sq. region is shown in (b) and (c). (b) The first layer of the ring shape discrete electrodes. The resistors and the location of the via's are indicated, (c) top view with second layer of ITO (floating electrode) visible, which hides the underneath electrode gaps and the resistors.

The lens fabrication process comprises photolithography, sputtering deposition, and standard LC cell assembly techniques. Figure 6 shows the top view of the steps involved in the top and bottom plate fabrication.

On the bottom plate, ITO-coated glass is patterned into rings with a resistor network in the first process step. Then, an insulator layer (SiO_2) is deposited by sputter coating on top of the patterned electrode layer. The insulator layer was subsequently patterned to include via connections using reactive ion etching. A nickel layer was then deposited using sputtering and patterned to include busline connections. Next, we deposited another insulator layer and subsequently an ITO layer via sputtering. The ITO layer was then patterned to be the floating electrodes. Following the floating electrode process, a thick insulator layer was deposited to reduce the edge effect of the floating electrodes. Finally, we spin-coated a polyimide layer (SE-2170) on the bottom plate and rubbed it after a soft baking and hard baking step. The SE-2170 PI layer provides ~3 deg of pretilt angle upon rubbing.

On the top plate, a continuous ITO was used as the ground plane. In the next step, deposited nickel is patterned to form the BM structure on top of reset boundaries to reduce light scattering from them. Then, PI is applied and rubbed in the antiparallel direction compared to the bottom plate.

After completing the process steps for the top and bottom plates, we assembled the two plates with precise alignment, following standard LCD assembly steps that include spraying silica spacers (20 μm diameter beads), dispensing sealing glue, pressing both plates, and curing the glue line. We then filled the LC using vacuum filling, and a flex cable was bonded to the nickel bus lines using anisotropic conductive tape (Fig. 7).

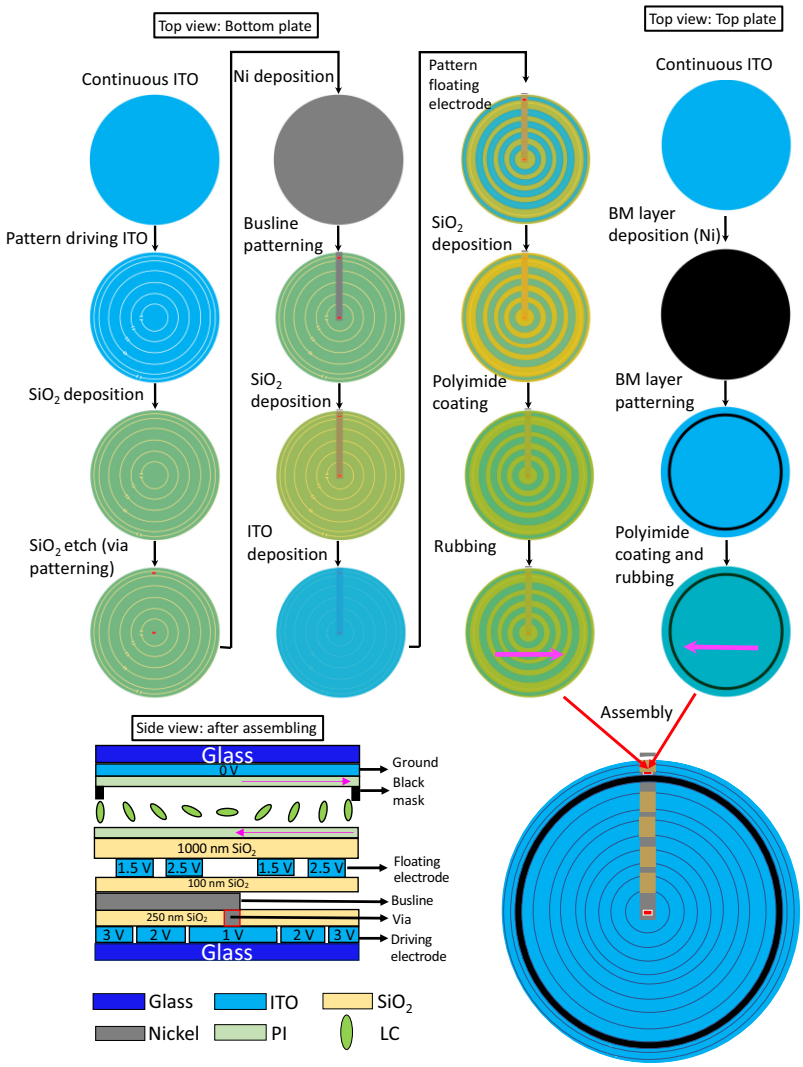

Fig. 6 Schematic diagram of step-by-step fabrication process (in top view). Processes are defined for each step. The side view of the layers of an assembled cell is shown in-side view on bottom left.

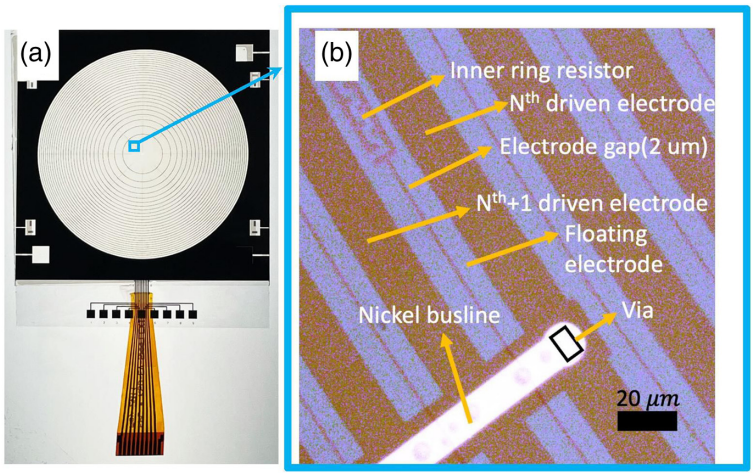

Fig. 7 Fabricated device and closer look at the features under reflective light condition.

5 Characterization

5.1 Phase Profile

The total phase retardation in the LC cell depends on the used voltage range from phase response curve. By assigning different voltage values on the buslines, the LC lens can be tuned to different optical power. In this paper, the phase profile of the device is shown in Figs. 8(a)–8(e), at +0.40 D optical configurations of the designed lens. The phase profile is obtained by passing white light through a color filter ($\lambda = 543.5$ nm) and the LC lens device placed at 45 deg between cross polarizers. The phase modulation of the fabricated cell is compared to an ideal lens phase modulation curve of equal optical power and shown in Fig. 8(f). Also, the measured phase profile across multiple segmented phase region is compared to a parabolic fit and shown in Fig. 8(g), where the position of the reset of SPP is indicated by black arrow mark.

5.2 Experimental Modulation Transfer Function measurement

The imaging resolution of the designed system for near-to-eye applications is investigated. For this purpose, we have used a negative chrome USAF test target, back illumined by fluorescent light box as the object. The image of the characterization is captured by a Canon Rebel XSi/450 D camera with 100 mm Canon lens. To mimic the near-eye application, the stack of LC lens/glass (SLG) is placed 2 cm away from the Canon camera lens. The SLG contains the built LC lens, a bias glass lens and a polarizer. As discussed above, the power of the LC lens switch between

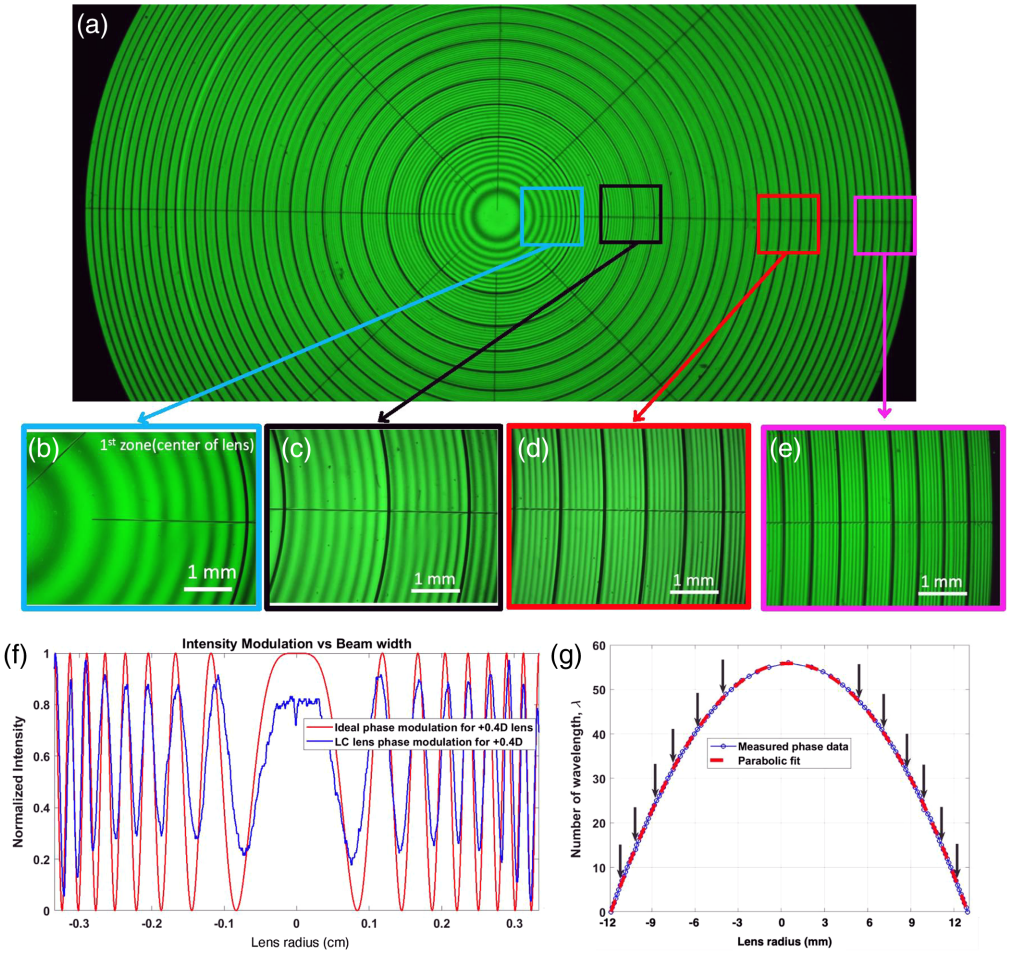

Fig. 8 (a) Phase profile of the lens within entire aperture (5 cm) for +0.40 D; (b)–(e) closer look at the four square region on the lens area indicated of (a); (f) comparison of position of interference fringes of the built LC lens device compared to an ideal lens, (g) comparison of the phase profile with respect to parabolic fit within multiple phase reset region. Black arrow mark indicates position of the phase reset on the phase profile.

−0.80 D and +0.80 D. A bias lens of +0.80 D is used to shift the tunable range to 0 D to 1.60 D. The polarization direction of the polarizer in the stack is parallel to the rubbing direction LC lens. The image of the USAF is taken with and without SLG in place. As with the modeling approach, imaging characterization is performed at five PPs to mimic human eye vision. However, to separate the contribution of the SPP in the imaging performance, data are presented separately for central vision and peripheral vision. We are considering the imaging performance for PP1 is central vision which corresponds to 0 deg gazing angle, there is no presence of SPP within this area. Imaging performance for PP2-PP5 are considered as peripheral vision as gazing angle is larger than 10 deg, there are presence of SPP within this area of the lens. For all the PP, a 5 mm wide physical aperture stop is used to mimic the human eye average pupil size.[28] The aperture stop is translated to be at a different redial distance from the center of the lens keeping the optical axis of the detector camera parallel to the lens normal- to represent different PPs. Image formed within the aperture area is captured by the Canon camera lens. While the physical aperture of width 5 mm is attached on the lens surface, the Canon camera lens aperture is wide open of size 35.71 mm ($f/2.8$, $f = 100$ mm).

Figure 9 shows the optical quality of LC lens for central vision considering PP1. In Fig. 9(a), image of the USAF chart is taken without the presence of SLG. Figure 9(b) shows the same target, but SLG is placed 2 cm away from the Canon camera lens and image is capture without altering any settings on the canon camera compared to Fig. 9(a) while the total power of the SLG is 1.60 D. Figure 9(c) shows the image when the operating condition remains the same as in Fig. 9(b), but the Canon camera lens focus ring is adjusted to find the best focus. Considering that the Canon camera lens is diffraction limited, Fig. 9(c) shows the image quality of the LC lens at central vision compared to the image quality without LC lens as shown Fig. 9(a).

Figure 10 shows the optical quality of LC lens for peripheral vision when human eye gaze to larger angle. In these cases, the effect of SPP degrades the image quality. Figures 10(a)–10(d) show the image of USAF as with same driving and detector setup discussed for Fig. 9(c), but the position of the 5 mm aperture stop on the lens is translated by 5, 10, 15, and 20 mm along same axis for Figs. 10(a)–10(d), respectively. As a result, Figs. 10(a)–10(d) represent image quality of the LC lens at 1.60 D optical power for PP2, PP3, PP4, and PP5, respectively.

To compare the measured MTF with the calculated MTF, we used two color filters in front of the white light source to assess the image quality for the monochromatic light. The wavelength of these color filters are 545 nm (λ_g) and 640 (λ_r), which results the phase step condition to be $16\lambda_g$ (full wave condition, best diffraction efficiency) and $13.5\lambda_r$ (half wave condition, worst diffraction efficiency), respectively. Figures 11(a)–11(e) show the closer look of the image quality of the LC lens for PP1-PP5, respectively, while imaging group (0) element (6) by placing the λ_g color filter. Figures 11(f)–11(j) show the closer look of the image quality of the LC lens for PP1-PP5, respectively, while imaging group (0) element (6) by placing the λ_r color filter. As with predicted simulation result, clear diffracted image is observable for the case of the λ_r color filter due to half-wave phase step condition. The angle between diffracted image increases for larger gazing angle, but experimentally it is observed that the diffracted image angle is within human eye resolution (1 arcmin = 0.0160 deg) up to PP3 even at worst case scenario. In Figs. 11(h)–11(j), the diffracted

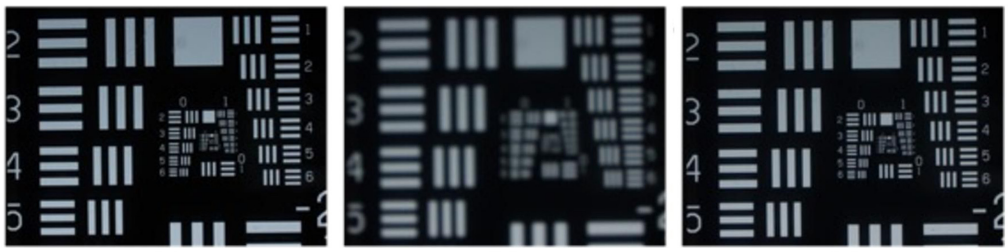

(a) (b) (c)

Fig. 9 Image resolution evaluation for central vision, (a) without SLG, (b) with SLG at ON state with optical power +1.60 D [camera focus is not adjusted compared to case (a)], (c) with SLG ON state with optical power +1.60 D after camera is adjusted to find the best focus.

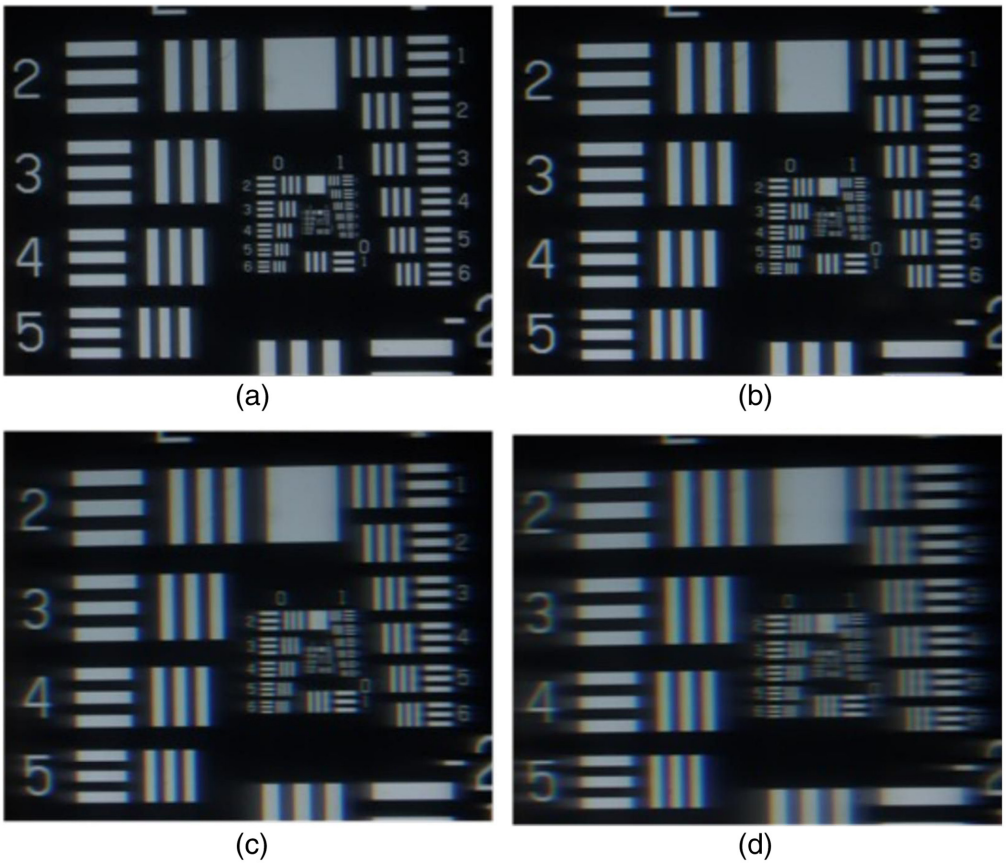

Fig. 10 Image resolution evaluation for peripheral view, (a)–(d) image resolution when SLG is placed with the optical power +1.60 D where center of gaze angle is at 14 deg (PP2).27 deg (PP3), 35 deg (PP4), 46 deg (PP5), respectively.

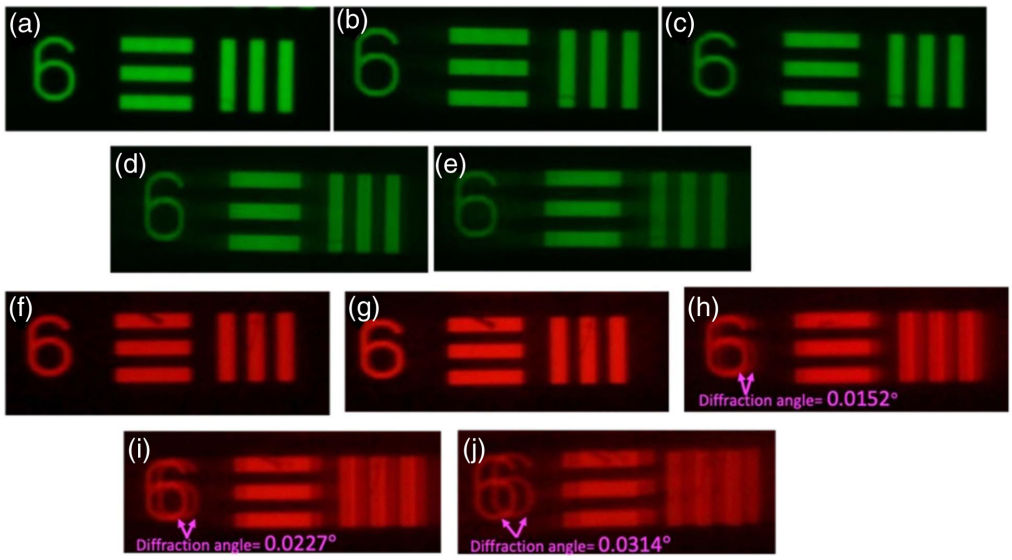

Fig. 11 Closer look at the captured image of group 0 element 6 of airforce chart using monochromatic light filter when optical power of SLG is +1.60 D. (a)–(e) The captured image with designed wavelength color filter ($\lambda_g = 545$ nm) for the case of PP1, PP2, PP3, PP4, PP5, respectively. (f)–(j) The image of the same object but with half-wavelength case color filter ($\lambda_r = 640$) nm for the case of PP1,PP2, PP3, PP4, PP5, respectively. Diffracted images are indicated by pink arrow and diffraction angles are written on the picture.

images are indicated by the pink color arrow and the measured angle of diffraction is written on each figure.

Although the discussed LC lens is considered for white light applications, the human eye is most sensitive to the green portion of the spectrum with peak sensitivity around 550 nm.[28] Considering the peak sensitivity of photopic vision, MTF is evaluated from the information resolution dimension data of USAF 1951 target with λ_g filter, and data of pixel size and a magnification factor of our camera. In the USAF 1951 chart, the spatial resolution for element 6 of group 0, when positioned at a specific distance from the detector, corresponds to a spatial frequency of 10 cycles per degree. The intensity modulation around the bar element 6 of group 0 is measured at five different PPs and shown in Fig. 12(a). To measure the MTF on those PPs, we have first calculated the contrast at eye chart bar. The contrast is defined as

$$\text{Contrast} = \frac{I_{\max} - I_{\min}}{I_{\max} + I_{\min}}, \tag{4}$$

where $I_{\max}$ and $I_{\min}$ represent the maximum and minimum pixel intensities near the test element, respectively. These intensities are measured in two scenarios: first, with the LC lens activated at maximum power (1.60 D), providing the contrast measurement for the LC lens; second, with the LC lens powered off, which corresponds to the contrast measurement for absolute black and white conditions. Finally, the MTF is measured after normalizing the measured contrast of the LC lens to baseline contrast of absolute black and white. The measured MTF at 10 cyc/deg is compared with the calculated MTF obtained from simulation for different gazing angles and shown in Fig. 12(b).

The MTF of human vision drops below 0.40 at a spatial resolution of 10 cycles per degree.[21,29] In contrast, the MTF measured in our device remains comparable to human eye resolution for viewing angles up to 30 deg.

5.3 Continuous Tunability and Experimental PSF Measurement

The designed example LC lens is continuously tunable between positive power (+0.80 D) and negative power (−0.80 D). To show continuous tunability, different voltage profiles for different optical power are measured and applied to the lens. Measured phase profile from the same area of the LC lens is shown in Fig. 13 at different tunable optical power configuration, from 0.10 D to 0.80 D optical power states in 0.10 D optical power increments. To get phase profile of the fabricated lens, the cell is placed at 45 deg between cross polarizer and white light passed though color filter of wavelength, $\lambda = 543.5$ nm.

To quantify the focusing capability of the lens with the tuned phase profile, experimental PSF is measured for different optical power. The measured spot profile forms an airy disk pattern. The first lobe diameter of the measured spot profile is compared with first lobe diameter of airy disk pattern of a diffraction limited lens. For this experiment, LC lens is stacked with a glass lens of 1.0 D. The image of the spot profile is captured at the calculated focal length of the total power of the LC lens and glass lens stack. Figures 14(a)–14(e) show the change of the spot profile size for the LC lens power 0 D, 0.20 D, 0.40 D, 0.60 D, 0.80 D, respectively. To measure the PSF, normalized intensity variation across the center of the spot profiles is calculated and shown in

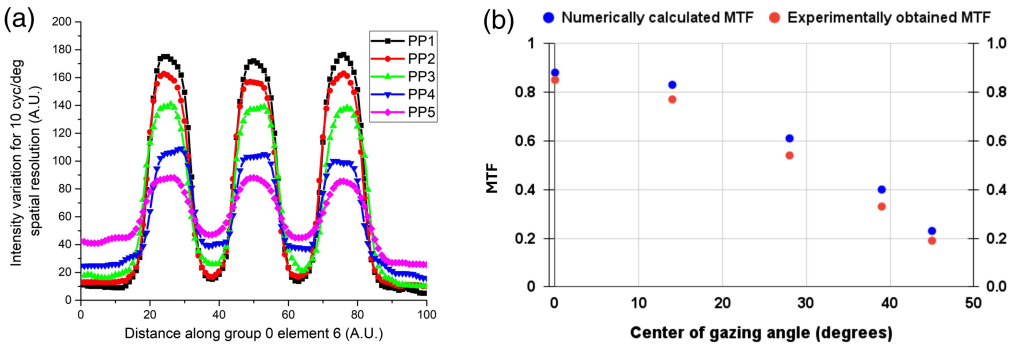

Fig. 12 (a) Green channel intensity modulation and (b) comparison of measured and simulated MTF at 10 cyc/deg spatial resolution for all PPs.

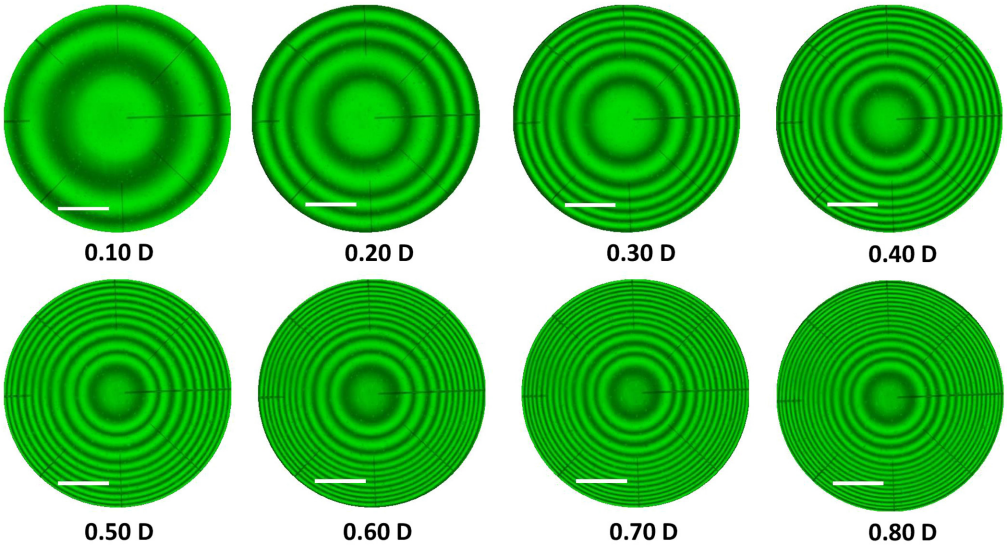

Fig. 13 Control over phase profile for different tunable optical power, seen from the same region area. Corresponding optical powers are indicated underneath of each phase profile. White bar indicates 2 mm length.

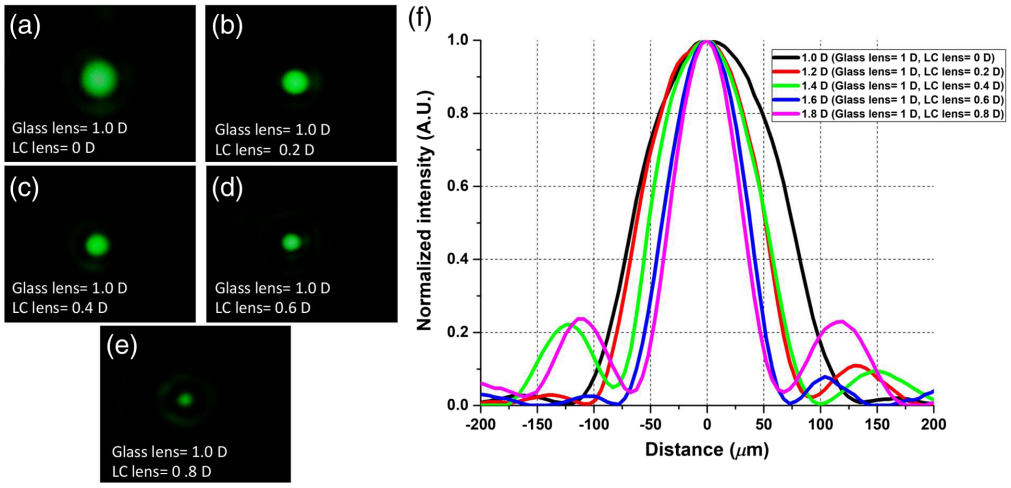

Fig. 14 Measured PSF at different optical power states. (a)–(e) The measured spot profile for LC lens power 0 D, 0.20 D, 0.40 D, 0.60 D, and 0.80 D, respectively. (f) Measured PSF for different optical power cases.

Table 1 Comparison of measured first lobe diameter of airy disk pattern compared to theoretical value.

Total optical power states	Measured first lobe diameter (μm)	Theoretical first lobe diameter of airy disk pattern (μm)
1.00 D	263	264
1.20 D	218	220
1.40 D	184	188
1.60 D	162	164
1.80 D	141	144

Fig. 14(f). Here, normalized intensity is equal to measured intensity values divided by the maximum intensity value. Width of the measured first lobe diameter is compared with the theoretical value of the first lobe diameter (q) of airy disk pattern, which is calculated from the following equation:

$$q = 2.44\frac{f\lambda}{D}.$$

Here, f, λ, and D represent the focal length, wavelength of light, and the aperture size, respectively. In our experimental case, $\lambda = 550$ nm and $D = 5$ mm. The measured q for different focal length of the LC lens shows good match with the theoretical value, which is summarized in Table 1.

6 Conclusion

In this paper, the design, modeling, fabrication, and characterization of an example 5 cm diameter tunable focus LC lens is discussed. The built device shows optical performance within human eye resolution up to 30 deg gazing angle, however, noticeable diffraction occurs in the peripheral vision. As the width of the segmented phase region becomes narrower, the angle of the diffraction becomes larger. Although the optical performance degrades for peripheral vision, high quality optical performance for the central vision will allow the application of the designed lens in many imaging systems and HMDs technologies.

Disclosures

The authors declare no conflict of interest.

Code and Data Availability

Additional data are available by contacting the authors.

Acknowledgments

The authors acknowledge support from Meta Reality Labs.

References

1. G. Kramida, "Resolving the vergence-accommodation conflict in head-mounted displays," *IEEE Trans. Vis. Comput. Graphics* **22**(7), 1912–1931 (2016).
2. J. Bailey et al., "Switchable liquid crystal contact lenses for the correction of presbyopia," *Crystals* **8**(1), 29 (2018).
3. H. S. Chen, M. S. Chen, and Y. H. Lin, "Electrically tunable ophthalmic lenses for myopia and presbyopia using liquid crystals," *Mol. Cryst. Liq. Cryst.* **596**(1), 88–96 (2014).
4. A. Jamali et al., "Large area liquid crystal lenses for correction of presbyopia," *Opt. Express* **28**, 33982–33993 (2020).
5. H. E. Milton et al., "Electronic liquid crystal contact lenses for the correction of presbyopia," *Opt Express* **22**(7), 8035–8035 (2014).
6. N. Hasan et al., "Adaptive optics for autofocusing eyeglasses," in *Opt. InfoBase Conf. Pap.*, Part F45-I, pp. 2016–2018 (2017).
7. G. Li et al., "Switchable electro-optic diffractive lens with high efficiency for ophthalmic applications," *Proc. Natl. Acad. Sci. U. S. A* **103**(16), 6100–6104 (2006).
8. N. Padmanaban, R. K. Konrad, and G. Wetzstein, "Autofocals: evaluating gaze-contingent eyeglasses for presbyopes," in *ACM SIGGRAPH 2019 Talks, SIGGRAPH 2019*, pp. 1–8 (2019).
9. L. Begel and T. Galstian, "Liquid crystal lens with corrected wavefront asymmetry," *Appl. Opt.* **57**(18), 5072–5072 (2018).
10. U. Mur, M. Ravnik, and D. Seč, "Controllable shifting, steering, and expanding of light beam based on multi-layer liquid-crystal cells," *Sci. Rep.* **12**(1), 352 (2022).
11. L. Chen et al., "Electrically tunable lenses: a review," *Front. Rob. AI* **8**, 678046 (2021).
12. C.-T. Lee et al., "Design of polarization-insensitive multi-electrode GRIN lens with a blue-phase liquid crystal," *Opt. Express* **19**(18), 17402–17407 (2011).
13. L. Li et al., "Near-diffraction-limited and low-haze electro-optical tunable liquid crystal lens with floating electrodes," *Opt. Express* **21**(7), 8371–8371 (2013).

14. L. Li, D. Bryant, and P. J. Bos, "Liquid crystal lens with concentric electrodes and inter-electrode resistors," *Liq. Cryst. Rev.* **2**(2), 130–154 (2014).
15. A. Jamali et al., "Design of a large aperture tunable refractive Fresnel liquid crystal lens," *Appl. Opt.* **57**(7), B10 (2018).
16. A. K. Bhowmick et al., "Haze reduction in concentric electrode-based large aperture liquid crystal lens with segmented phase profile," *Opt. Eng.* **62**(8), 085101 (2023).
17. F. Yun-Hsing et al., "Liquid crystal microlens arrays with switchable positive and negative focal lengths," *J. Disp. Technol.* **1**(1), 151–156 (2005).
18. Y. H. Lin, Y. J. Wang, and V. Reshetnyak, "Liquid crystal lenses with tunable focal length," *Liq. Cryst. Rev.* **5**(2), 111–143 (2017).
19. H. Cheng, A. Bhowmik, and P. Bos, "Fast-response liquid crystal variable optical retarder and multilevel attenuator," *Opt. Eng.* **52**(10), 107105 (2013).
20. H. Nakamura, J. Crain, and K. Sekiya, "Optimized active-matrix drives for liquid crystal displays," *J. Appl. Phys.* **90**(5), 2122–2127 (2001).
21. A. B. Watson, "A formula for the mean human optical modulation transfer function as a function of pupil size," *J. Vision* **13**(6), 18 (2013).
22. D. G. Voelz, *Computational Fourier Optics: A MATLAB Tutorial*, SPIE Press, Bellingham, Washington (2011).
23. T. Zhan et al., "Practical chromatic aberration correction in virtual reality displays enabled by cost-effective ultra-broadband liquid crystal polymer lenses," *Adv. Opt. Mater.* **8**(2), 1901360 (2020).
24. B. Kress, "Digital optical elements and technologies (EDO19): applications to AR/VR/MR," *Proc. SPIE* **11062** (2019).
25. L. Li et al., "Near-diffraction-limited tunable liquid crystal lens with simplified design," *Opt. Eng.* **52**(3), 035007 (2013).
26. N. A. Riza and M. C. DeJule, "Three-terminal adaptive nematic liquid-crystal lens device," *Opt. Lett.* **19**(14), 1013 (1994).
27. A. F. Naumov et al., "Control optimization of spherical modal liquid crystal lenses," *Opt. Express* **4**(9), 344 (1999).
28. E. Hecht, *Optics*, Addison-Wesley (2001).
29. D. R. Williams et al., "Double-pass and interferometric measures of the optical quality of the eye," *J. Opt. Soc. Am. A* **11**(12), 3123–3123 (1994).

Amit K. Bhowmick received his MS degree in chemical physics from Kent State University in 2020 and his PhD in chemical physics from Kent State University in 2023. His current research interest is liquid-crystal optical devices, such as liquid-crystal lenses.

Afsoon Jamali received her MS degree in chemical process engineering from the University College London in 2010 and was a research assistant at KU Leuven, before joining Kent State University. She received her PhD from Liquid Crystal Institute, Kent State University. Her current research interests include liquid-crystal devices specifically liquid-crystal lenses and beam-steering devices.

Douglas Bryant is a display engineering manager at Kent State University. He received his MS degree in electrical engineering from the University of Southern California in 1992. His research focus is the design and fabrication of liquid-crystal devices.

Sandro Pintz received his MS degree in electrical engineering from the Universidad de Chile. He has obtained further graduate degrees in electrical engineering from the University of Wisconsin-Madison. His research interest lies on various applications in display technology and optics.

Philip J. Bos is a professor of physics and member of the Liquid Crystal Institute at Kent State University. He received his PhD in physics from Kent State University in 1978, before joining Tektronix Inc., and then returning to Kent State in 1994. His research focus is optical applications of liquid crystals.